Energy exchanges in Saturn's polar regions from Cassini observations: Part I: Eddy-zonal flow interactions

Peter L. Read[1], Arrate Antuñano[2,3], Simon Cabanes[4], Greg Colyer[1], Teresa del Río Gaztelurrutia[3], and Agustin Sanchez-Lavega[3]

[1]Atmospheric, Oceanic and Planetary Physics, Department of Physics, University of Oxford, Clarendon Laboratory, Parks Road, Oxford, OX1 3PU, UK
[2]School of Physics and Astronomy, University of Leicester, University Road, Leicester, LE1 7RH, UK
[3]Dpto de Física Aplicada, Escuela de Ingeniería de Bilbao, UPV/EHU, Spain
[4]DICEA, Sapienza Università di Roma, Via Eudossiana, 18 - 00184, Rome, Italy

Key Points:

- Velocity fields obtained from Cassini images are analysed to determine eddy-zonal exchanges of kinetic energy in Saturn's polar regions.
- Both the North and South Polar jets at 76°N and 70°S are energised from non-axisymmetric eddies, including the North Polar Hexagon.
- The North Polar Vortex was barotropicallly unstable at this time, but the South Polar Vortex was gaining kinetic energy from eddies.

Corresponding author: Peter L. Read, peter.read@physics.ox.ac.uk

Abstract

Saturn's polar regions (polewards of $\sim 63^\circ$ planetocentric latitude) are strongly dynamically active with zonal jets, polar cyclones and the intriguing north polar hexagon wave. Here we analyse measurements of horizontal winds, previously obtained from Cassini images by Antuñano et al. (2015), to determine the spatial and spectral exchanges of kinetic energy (KE) between zonal jets and eddies in Saturn's polar regions. As previously found for lower latitudes on Saturn, eddies of most resolved scales generally feed KE into the eastward and westward zonal jets at mean rates between 4.4 $\times 10^{-5}$ and 1.7 $\times 10^{-4}$ W kg^{-1}. In particular, the north polar jet (at 76°N) was being energised at a rate of $\sim 10^{-4}$ W kg^{-1}, dominated by the contribution due to the zonal wavenumber $m = 6$ north polar hexagon wave itself. This implies that the hexagon was not driven through a barotropic instability of the north polar jet, but may suggest a significant role for baroclinic instabilities or other internal energy sources for this feature. The south polar jet KE was also being sustained by exchanges from eddies in that latitude band across a wide range of m. In contrast, results indicate that the north polar vortex may have been barotropically unstable at this time with eddies of low m gaining KE at the expense of the axisymmetric cyclone. However, the southern polar cyclone was gaining KE from the non-axisymmetric eddies at this time, including $m = 2$ and its harmonics, as the elliptical distortion of the vortex may have been decaying.

Plain Language Summary

Saturn's polar regions (polewards of $\sim 63^\circ$ latitude) are strongly meteorologically active with high speed eastward and westward zonal jets, intense, hurricane-like polar cyclones and the intriguing north polar hexagon wave. Here we analyse measurements of horizontal winds, previously obtained by tracking features in images from the Cassini Orbiter spacecraft, to determine how kinetic energy is exchanged between the zonal jets and various types of eddy. As measured previously at low- and mid-latitudes on Jupiter and Saturn, we found that Saturn's north and south polar jets were gaining energy at the expense of the smaller scale eddies, including the northern polar hexagon itself. This means that the hexagon must likely have been driven by processes below the clouds, probably involving buoyancy forces associated with thermal gradients in the atmosphere, much like the mid-latitude cyclone-anticyclone weather systems on Earth. Energy exchanges within the polar vortices themselves were more complicated, with the northern vortex apparently losing energy to wavy distortions of the vortex, but with the southern vortex gaining energy from an elliptical distortion of the vortex core.

1 Introduction

Since the Cassini orbiter mission to Saturn, it has been clear (Sánchez-Lavega et al., 2006; Dyudina et al., 2008, 2009; Baines et al., 2009; Antuñano et al., 2015; Sayanagi et al., 2015, 2018) that its polar regions are dominated at the cloud-top levels by intense, cyclonic vortices, centred on each pole, surrounded by an additional eastward jet stream at latitude 70° S and 76° N respectively (planetocentric). The polar vortices in both hemispheres extend to a radius of around 5° latitude, corresponding to around 4700 km (Sánchez-Lavega et al., 2006; Sayanagi et al., 2015), with strong circumpolar jets peaking at around 87° latitude with velocities of up to 160 - 175 m s^{-1}. The vortices appear to be roughly circular, with spiral cloud bands and an apparent clearing at the centre of each vortex, reminiscent of terrestrial tropical cyclones. But high resolution images (Sánchez-Lavega et al., 2006; Dyudina et al., 2008, 2009; Baines et al., 2009; Sayanagi et al., 2015) indicate many small-scale cloudy features that break the circular symmetry.

Weak westward zonal flow is found immediately beyond the edge of each polar vortex, reversing at lower latitudes to form the secondary eastward circumpolar jets (South Polar Jet and North Polar Jet; SPJ and NPJ) at approximately 70° and 76° planetocentric latitude[1] in the southern and northern hemispheres respectively before reversing again at even lower latitudes. The NPJ is notable for its regular hexagonal shape, first discovered in Voyager images by Godfrey (1988). This North Polar Hexagon (NPH) feature has evidently persisted to the present day, and was observed in detail by the Cassini orbiter (e.g. Baines et al., 2009; Fletcher et al., 2018) in both cloud motions and in the retrievals of temperature in the lower stratosphere from Cassini Composite Infrared Radiometer (CIRS) measurements. Such a polygonal perturbation to the jet is not seen in the SPJ (Sánchez-Lavega et al., 2002), however, for reasons that are still poorly understood.

Indeed the nature and origin of both the polar cyclones and the NPH continues to pose major challenges to atmospheric scientists (see Sayanagi et al., 2018, for a recent review), prompting a continuing need for more observational information with which to constrain theories and models. The resemblance of the polar vortices to terrestrial hurricanes, for example, would suggest a need for localised heating e.g. produced by latent heat release in moist convection (e.g. O'Neill et al., 2015, 2016; Sayanagi et al., 2015). But the compact morphology of terrestrial tropical cyclones is due in part to concentrated convergence and upwelling associated with the underlying ocean surface (e.g. Montgomery & Smith, 2017), which is likely absent on Saturn.

The NPH has been the subject of much discussion since its discovery, not least because of its remarkable symmetry and stable persistence over several decades. Initial studies noted a possible association between the hexagon wave and a large anticyclonic vortex, known as the North Polar Spot (NPS), lying just outside the main jet at the time of the Voyager encounters (Godfrey, 1988), suggesting that the anticyclone was perturbing the circumpolar jet to induce a train of Rossby waves with a wavelength just matching the wavenumber $m = 6$ pattern at this latitude (Allison et al., 1990; Sánchez-Lavega et al., 1997). Subsequent observations from the Hubble Space Telescope showed that the NPS persisted into the 1990s, but by the time the Cassini Orbiter arrived at Saturn it had disappeared. Cassini observations, however, showed that the NPH was still present even without the presence of the NPS, implying that the hexagon wave was not being maintained by the NPS.

More recent explanations proposed for the origin of the NPH attribute it either to a Rossby wave propagating upwards from a (nearly stationary) source in the deep interior (Sánchez-Lavega et al., 2014) or to an equilibrated instability (barotropic or baroclinic) of either a relatively shallow NPJ itself (e.g. Aguiar et al., 2010; Morales-Juberías et al., 2011, 2015; Farrell & Ioannou, 2017) or deep jets driven by deep planetary convection (Garcia et al., 2020; Yadav & Bloxham, 2020). The formation of polygonal jet flows as the fully developed form of either barotropic or baroclinic instabilities is well known in laboratory experiments (e.g. Hide & Mason, 1975; Sommeria et al., 1989, 1991; Bastin & Read, 1998; Früh & Read, 1999; Aguiar et al., 2010) though are much less commonly found in planetary atmospheres (however, cf Yadav & Bloxham, 2020). Equilibrated barotropic instabilities of plausible zonal jets were commonly found to be associated with chains of cyclonic or anticyclonic vortices alternately inside and outside of the meandering jet (Aguiar et al., 2010; Morales-Juberías et al., 2011; Yadav & Bloxham, 2020), which are not observed prominently on Saturn (Antuñano et al., 2015), though such features could conceivably be very weak or imperceptibile in some model parameter regimes with more complex vertical structure (e.g. Morales-Juberías et al., 2015). Baroclinic instabilities in stably-stratified flows may also lead to equilibrated meandering polygonal jet structures at certain levels in the vertical, with or without accompanying vortices (e.g. Bastin & Read, 1997, 1998). Such regimes may persist for as long as the initial jet is maintained, and a plausible complete solution comprising a jet, sustained by upscale kinetic energy transfers from small-scale eddies, which in turn devel-

[1] Note that all latitudes in this paper are planetocentric.

ops a large-scale polygonal, meandering, wave-like barotropic instability, has been demonstrated in a two-layer numerical simulation by Farrell & Ioannou (2017). Such a "flux loop" mechanism emulates aspects of a similar scenario in two-dimensional stratified turbulence identified by Boffetta et al. (2011).

Observations have indicated that the maintenance of alternating jet flows on Saturn, at least at extra-tropical middle latitudes, is associated with strongly divergent or convergent Reynolds stresses that directly accelerate the zonal flow (Del Genio et al., 2007; Del Genio & Barbara, 2012) in a spectrally non-local transfer of kinetic energy (KE). This is similar to what has been found at mid-low latitudes in Jupiter's atmosphere, with an inferred mean transfer rate of $\sim 10^{-5} - 10^{-4}$ W kg^{-1}. The sign and magnitude of the conversion rate of eddy kinetic energy at latitudes higher than $\pm 60°$ has not so far been determined (for either planet). Similarly, exchanges of kinetic energy between the NPH wave and other components of the flow have yet to be determined. Yet such statistics may shed important light on the nature of the NPH and other features at these high latitudes and provide important constraints on plausible models of these phenomena.

In the present work, therefore, we extend the analysis of the velocity field measurements of Antuñano et al. (2015) to explore the zonal kinetic energy spectra of both polar regions of Saturn and estimate the sign and magnitude of the rates of exchange of kinetic energy between different scales of motion. The data prove sufficient to obtain robust estimates of the total eddy-zonal conversion rate of KE for both polar regions and more locally in the vicinity of the SPJ, NPJ and both polar vortices. A zonal spectral decomposition of this conversion rate also allows a determination of the interaction between the NPH and the NPJ and other features.

Section 2 summarises the observations used and the methods applied to obtain the KE spectra. Section 3 describes the methods used to compute the eddy-zonal KE conversion rates and spectral and spatial fluxes. Section 4 presents the results on the eddy-zonal flow energy exchanges, including regional variations and their spectral decomposition.The results and their significance are discussed in Section 5 together with conclusions and suggestions for further work.

2 Observations

The observations used in the present study consist of two maps of horizontal velocities in Saturn's northern and southern hemispheres, as previously published by Antuñano et al. (2015). As fully described in that paper, these measurements were derived from sets of Cassini Imaging Sub-System (ISS) Wide Angle Camera (WAC) and Narrow Angle Camera (NAC) images using the continuum band CB2 and CB3 filters, acquired for the northern hemisphere in June 2013 and for the southern hemisphere using WAC CB2 and CB3 images taken in October 2006 and December 2008. Additional NAC images using the CB2 and red filters taken in July 2008 were also used to analyse the southern polar vortex. The WAC images covered a region extending from a planetocentric latitude of around 60-65° to each pole (apart from a segment in longitude between around 35° - 110°W) with a horizontal resolution equivalent to around 0.05° latitude (around 50km) per pixel, while NAC images were mostly used for the polar vortices, with a resolution equivalent to around 0.01° latitude (around 10 km) per pixel.

2.1 Velocity measurements

Horizontal velocities were obtained using semi-automated image correlation methods (i.e. involving some manual intervention, see Hueso et al., 2009; Sánchez-Lavega et al., 2019, for details) between pairs of images separated in time by intervals of approximately 1-10 hours. The correlation algorithm used pixel box sizes of 23×23 (in the north) or 25×25 (in the south), leading to a spatial resolution of the velocity vectors equiv-

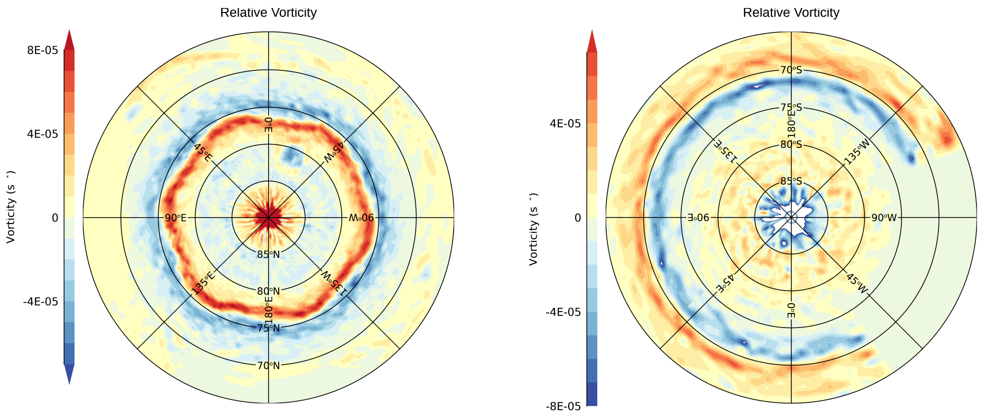

(a) Relative vorticity (N) ζ.

(b) Relative vorticity (S) ζ.

Figure 1: Cloud-top level vorticity fields, obtained from cloud-tracked wind measurements using Cassini ISS images by Antuñano et al. (2015), for Saturn's (a) north polar and (b) south polar regions. Note that velocity vectors were not available in the south equatorwards of 76°S between longitudes of $\sim$ 35°-110°W.

alent to around 1° latitude or 1000 km outside the polar vortices, reducing to around 0.2° or 200 km within the polar vortices themselves. The automatically generated velocity vectors were supplemented by a small number (around 1% of the total) of vectors obtained manually from the motion of visually identified cloud tracers. The estimated measurement uncertainty on each vector was around 5-10 m s^{-1}.

Figure 1 shows the maps of the relative vorticity in (a) the northern and (b) the southern hemispheres. These maps clearly show the regular, symmetrical North Polar Hexagon feature centred on the eastward jet at 76° N, the corresponding near-circular eastward jet centred at 71° S and the intense cyclonic polar vortices in each hemisphere. Zonal motion at intermediate latitudes is generally westward (relative to Saturn's System III; Desch & Kaiser (1981); Seidelmann et al. (2007); Archinal & et al. (2018)) but less strongly concentrated into clear jets. For the present study, the original velocity vectors from Antuñano et al. (2015) were interpolated onto a regular latitude-longitude grid using convex hulls and Delauney triangulation via the QHULL routine of the Interactive Data Language (IDL). The final dataset was held on a grid separated by 3° in longitude and 0.23° in latitude. This almost certainly leads to some oversampling in latitude, so fields were typically smoothed to a latitudinal resolution of around 1°.

2.2 Zonal mean velocities

The use of a regular latitude-longitude grid makes it easier, among other things, to compute zonal averages. Figure 2 shows profiles of the zonal mean zonal velocity $\overline{u}$ in (a) the north and (b) the south, computed from the velocities on the new longitude-latitude grid. This clearly shows the strong eastward jets at 76° N and 71° S and the complex profile across the polar vortices. Both sets of jets are well resolved, with peak velocities of the North and South Polar Jets (NPJ and SPJ) around 100 and 80 m s^{-1} respectively. The zonal mean structure of the polar vortices indicates peak velocities of around 140 m s^{-1} in both hemispheres with complex "shoulders" on the equatorward side of each vortex that differ markedly between the north and south. This is slightly weaker in the south than shown by Antuñano et al. (2015), likely due to some implicit

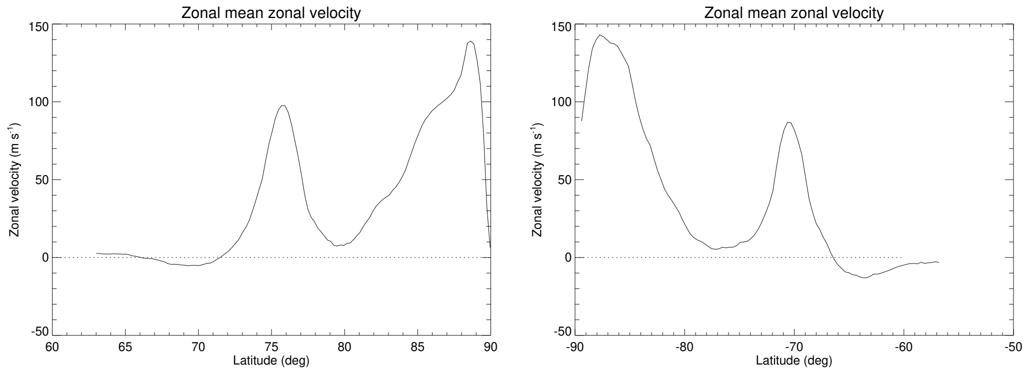

(a) Mean Zonal Velocity (N) $\overline{u}$. (b) Mean Zonal Velocity (S) $\overline{u}$.

Figure 2: Zonal mean zonal velocity profiles, obtained from Cassini ISS images by Antuñano et al. (2015) and reinterpolated in the present work onto a regular longitude-latitude grid, for Saturn's (a) north polar and (b) south polar regions.

smoothing in the interpolation used here to a somewhat lower resolution compared to the earlier study.

2.3 Eddy kinetic energy

On subtracting the zonal mean velocities from the original velocity field, we can then calculate variances and covariances of the residual eddy components. Figure 3 shows the profiles of specific eddy kinetic energy (EKE), defined as

$$K_E = \frac{1}{2}(\overline{u'^2} + \overline{v'^2}), \tag{1}$$

as a function of latitude in each hemisphere, where primed quantities represent departures from the zonal mean (denoted by the overbar). This exhibits markedly different behaviour between each hemisphere, with much larger peak values of K_E in the north compared with the south. In particular, there is a pronounced double peak in K_E centred on the latitude of the NPJ, corresponding to the strong NPH hexagonal wave that modulates both u and v in longitude. An even stronger peak in K_E exceeding 500 m^2 s^{-2} is seen at the inner edge of the North Polar Vortex (hereafter NPV), indicating a strong departure of the vortex from a circular shape. Although a somewhat similar trend is seen with the south polar vortex it is much weaker (< 200 m^2 s^{-2}) and more widely spread in latitude. These apparent peaks so close to each pole might be accentuated by possible small systematic errors in location due to the interpolation method used here, although this is hard to quantify. There is also evidence for a weak and broad peak in K_E around the latitude of the SPJ but mostly < 100 m^2 s^{-2}.

2.4 Eddy length scales

Given profiles of K_E we can then calculate estimates of quantities such as the Rhines wavelength scale λ_R, representing a cross-over scale between large-scale waves and small-scale turbulence (e.g. Vasavada & Showman, 2005; Chemke & Kaspi, 2015; Vallis, 2017) and defined in terms of K_E by

$$\lambda_R \simeq 2\pi \left(\frac{\sqrt{K_E}}{\beta} \right)^{1/2}, \tag{2}$$

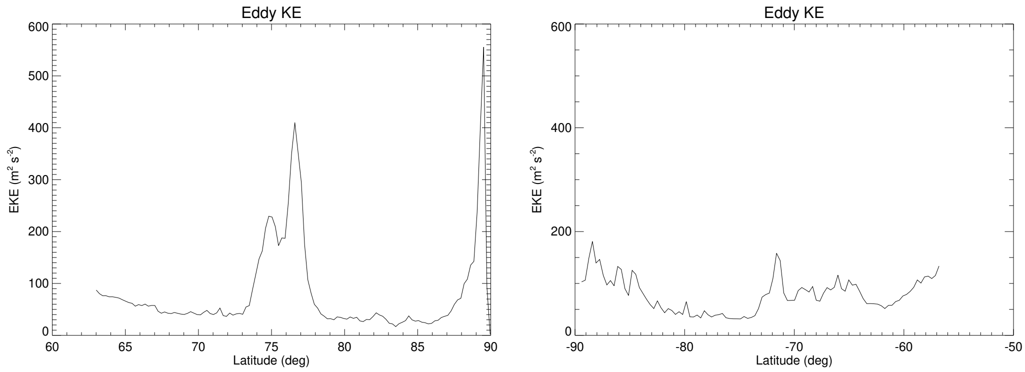

(a) EKE (N) (b) EKE (S)

Figure 3: Profiles of EKE for Saturn's (a) north polar and (b) south polar regions.

where $\beta = (1/a)df/d\phi$ is the northward gradient of the Coriolis parameter, $f = 2\Omega \sin\phi$, with latitude ϕ. This typically represents a scale comparable to the distance between eastward or westward zonal jet maxima in geostrophic turbulence (e.g. Vasavada & Showman, 2005; Chemke & Kaspi, 2015; Vallis, 2017). This scale may also be compared with other length scales, such as Saturn's mean radius ($a = 5.823\times10^4$ km) and scales representative of energetic eddies, such as the first baroclinic Rossby radius of deformation, L_D. The latter is defined as a wavelength here by

$$\lambda_D = 2\pi L_D \simeq 2\pi \left(\frac{NH}{f}\right), \tag{3}$$

where N is the mean buoyancy or Brunt-Väisälä frequency, H is a vertical scale height (often taken somewhat arbitrarily to be the pressure scale height near 1 bar pressure). For Saturn, N is not well measured beneath the visible clouds though likely varies greatly with depth, and H is also not known with much confidence. L_D was estimated by Read et al. (2009) from measurements of Saturn's potential vorticity configuration near the cloud tops to vary approximately with latitude as $L_D \simeq 1500/\sin\phi$ km, so here we take

$$\lambda_D \simeq 3000\pi/|\sin\phi| \quad \text{km}. \tag{4}$$

Profiles of λ_R and λ_D, calculated using Eqs (2) and (4), are shown in Figure 4 for (a) the north and (b) the south. These show that both λ_R and λ_D are mostly much smaller than the planetary radius a and indicate how λ_R diverges to very large scales as each pole is approached (since $\beta \to 0$ as $|\phi| \to 90°$), while λ_R increases slowly with ϕ away from the pole. λ_R and λ_D are comparable around latitude $\phi \sim 60-65°$ in each hemisphere, indicating that λ_D may tend to be similar to or larger than λ_R equatorward of around 60°. There are local variations in λ_R, however, especially close to the NPJ, indicating that variations in λ_D/λ_R may be found elsewhere. But in general this suggests that Saturn's mid-high latitude regions are characterised by values of λ_D that are smaller than λ_R. It is also of interest to note that λ_R is comparable to the separation distance between the NPJ and SPJ and the adjacent eastward jets on the equatorward sides. λ_D at 76°N is around 10^4 km and corresponds to a longitudinal wavenumber of around $m =$ 9 and is somewhat larger than the FWHM of the north polar hexagon at around 5800 km.

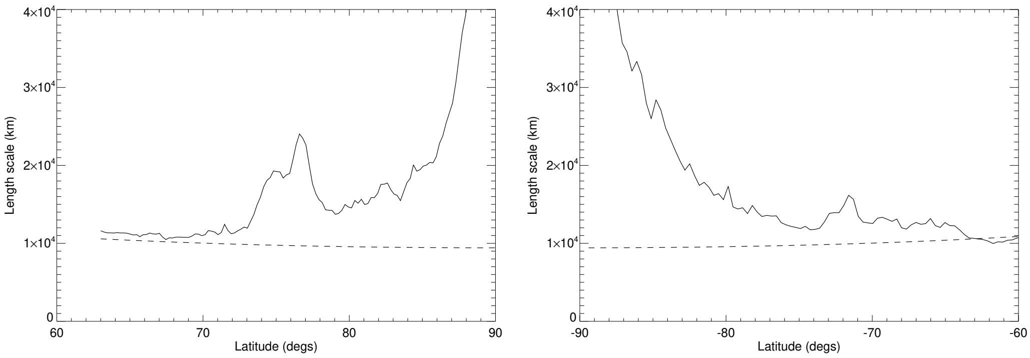

(a) Key lengthscales (North) (b) Key lengthscales (South)

Figure 4: Key lengthscales computed for Saturn's north polar (a) and south polar regions (b). Solid line is the Rhines wavelength scale λ_R, while the dashed line shows estimates of the wavelength λ_D corresponding to the first baroclinic Rossby radius of deformation L_D (see text).

3 Analysis methods

In this section we outline the diagnostics used to examine the properties of the polar circulations on Saturn, with particular reference to the transfer of KE between different scales of motion.

3.1 Eddy-zonal flow interactions

The forcing of zonal jets by eddies is commonly discussed in terms of the zonal mean zonal momentum equation, which can be written

$$\frac{\partial \overline{u}}{\partial t} - (f + \overline{\zeta})\overline{v} + \overline{w}\frac{\partial \overline{u}}{\partial z} = -\frac{1}{\rho_0}\nabla.\mathbf{F_m} + \overline{\mathcal{F}}, \tag{5}$$

(e.g. Andrews et al., 1987), where $\overline{\zeta}$ is the vertical component of zonal mean vorticity, $\overline{v}$ and $\overline{w}$ are the zonal mean meridional and vertical velocity components (where $\overline{v} > 0$ is northward in both hemispheres) and $\overline{\mathcal{F}}$ represents frictional effects and body forces acting on the flow. $\mathbf{F_m}$ represents the eddy flux of zonal momentum in the meridional (ϕ, z) plane due to the Reynolds stresses. In spherical coordinates, $\nabla.\mathbf{F_m}$ can be written

$$\frac{1}{\rho_0}\nabla.\mathbf{F_m} = -\frac{1}{a\cos^2\phi}\frac{\partial}{\partial\phi}(\overline{u'v'}\cos^2\phi) - \frac{1}{\rho_o}\frac{\partial}{\partial z}(\rho_0\overline{u'w'}). \tag{6}$$

where $\rho_0(z)$ is a background reference density profile, so $\mathbf{F_m}$ becomes

$$\mathbf{F_m} = -\rho_0\cos\phi[\overline{u'v'}, \overline{u'w'}]. \tag{7}$$

For the present problem we have no direct information on vertical velocity, other than to anticipate that it is likely to be much smaller than typical horizontal velocities (by a factor O($Ro.H/L$), where Ro is the Rossby number and H and L are vertical and horizontal lengthscales). So we will focus here on the horizontal eddy fluxes and the Reynolds stress divergence contribution to the energy budget.

The rate of conversion of kinetic energy between eddies and zonal mean flow is typically calculated from Eq (5), integrating in latitude (and height) across the domain. Neglecting the vertical dimension in the present context, we can calculate the rate of increase of zonal mean KE, denoted by K_Z as

$$\frac{dK_Z}{dt} = C(K_E, K_Z) \tag{8}$$

$$= -\frac{\int \left[\frac{\overline{u}}{a\cos\phi}\right] \frac{\partial}{\partial\phi}(\overline{u'v'}\cos^2\phi)d\phi}{\int \cos\phi d\phi} \tag{9}$$

$$= \frac{\int \frac{\partial}{\partial\phi}\left[\frac{\overline{u}}{a\cos\phi}\right] \overline{u'v'}\cos^2\phi d\phi}{\int \cos\phi d\phi}, \tag{10}$$

neglecting boundary terms in the usual way (cf Peixóto & Oort, 1974), where $C(K_E, K_Z)$ represents the corresponding conversion rate of eddy KE (K_E) to K_Z.

This formulation considers just the interaction between the zonal jet flow and non-axisymmetric eddies of all scales. The $C(K_E, K_Z)$ term can, however, be decomposed further into contributions from different zonal harmonics of wavenumber index m via a Fourier analysis of u' and v' in longitude (cf Chemke & Kaspi, 2015). Given the complex amplitude spectra of u' and v', denoted here by $\tilde{u'}$ and $\tilde{v'}$, the relevant self-interaction component of the Reynolds stress becomes

$$\widetilde{u'v'}(m,\phi) = \tilde{u'}(m,\phi)\tilde{v'}^*(m,\phi) + \tilde{u'}^*(m,\phi)\tilde{v'}(m,\phi), \tag{11}$$

where starred quantities represent complex conjugates. We can thus obtain the spectrally decomposed eddy-zonal KE conversion rate by extension of Eq (9) using Eq (11),

$$C\widetilde{(K_E, K_Z)}(m) = \frac{\int \left[\frac{\overline{u}}{a\cos\phi}\right] \partial/\partial\phi(\widetilde{u'v'}(m,\phi)\cos^2\phi)d\phi}{\int \cos\phi d\phi}, \tag{12}$$

In our analyses below, therefore, we include computations of both $C(K_E, K_Z)$ and $C\widetilde{(K_E, K_Z)}(m)$, integrated over various ranges in latitude and locally as a function of ϕ.

4 Eddy-zonal flow interactions

In this section we present the results of analysing the rates of conversion between eddy and zonal mean KE in the vicinity of both polar regions of Saturn. Calculations include both the total conversion rate averaged over the whole polar region $|\phi| > 60°$ and particular subranges of ϕ to focus on both polar vortices and the NPJ and SPJ.

4.1 Total conversion rates

Given the gridded velocity fields described in Section 2 above, it is straightforward to compute the northward flux of eddy momentum, $\overline{u'v'}$, at each latitude row to obtain the profiles presented in Figure 5. The unfiltered results are somewhat noisy but there are clear features in the profiles at the locations of both polar vortices and around the latitudes of the north and south polar jets. Fig. 5 also shows dashed profiles of the zonal mean wind $\overline{u}$ (scaled by 1/5) in each hemisphere for reference. This shows some complex structure around the polar vortices, but with clear changes of sign of $\overline{u'v'}$ close to the cores of both the NPJ and SPJ.

Calculating nominal values of $C(K_E, K_Z)$ from either Eq (9) or (10), without any explicit smoothing in latitude and integrating over the full range in latitude for each hemisphere, we obtain the mean KE conversion rate from eddies into the zonal jet, with the results shown in the first two row of Table 1. This shows a general trend for eddies to be transferring KE into the zonal jets in both polar regions, though with at around three

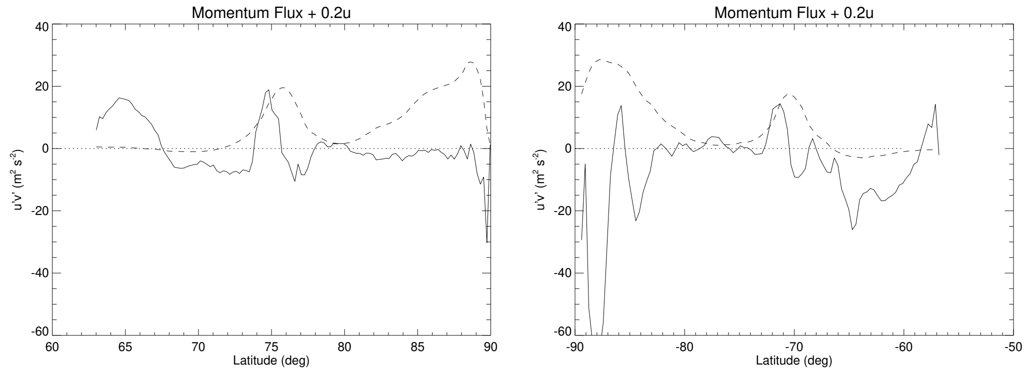

(a) Eddy momentum flux (N) u. (b) Eddy momentum flux (S) v.

Figure 5: Profiles of eddy momentum flux, $\overline{u'v'}$, smoothed in latitude to a resolution of 1° for Saturn's (a) north polar and (b) south polar regions. Dashed lines show the corresponding profiles of $\overline{u}$ scaled by 1/5. Note that different scales are used for the axes in the plots in (a) and (b) to show the features more clearly.

times the rate in the south compared with the north, at least at the time when these observations were acquired. The uncertainties are estimated roughly from the spread of calculations using either Eq (9) or (10) and over variations in the latitude range and different levels of smoothing in latitude, though this should probably be considered a lower limit on the uncertainty in each case.

Table 1: Eddy-zonal flow kinetic energy conversion rates on Saturn, computed over different latitude ranges using the area-weighted mean of the Lorenz form defined in Eq (10) and the local Reynolds stress divergence defined in Eq (9) from the dataset of Antuñano et al. (2015).

Feature	Latitude range (°)	$C(K_E, K_Z)$ (W kg^{-1})
North polar region	66° – 90°N	5.2 ±0.6 × 10^{-5}
South polar region	66° – 90°S	1.7 ±0.2 × 10^{-4}
North polar jet	70° – 79°N	1.2 ±0.1 × 10^{-4}
South polar jet	66° – 76°S	1.4 ±0.2 × 10^{-4}
North polar vortex	85° – 90°N	-3.3 ±1.1 × 10^{-5}
South polar vortex	80° – 90°S	4.1 ±0.2 × 10^{-4}

4.2 Regional conversion rates

If we focus attention on particular features or regions, it is of interest to evaluate the contribution of the northern and southern polar jets and the polar vortices to the overall transfer of KE from eddies to zonal flow in each polar region. The juxtaposition of the peaks and troughs of $\overline{u'v'}$ in Fig. 5 with the profile of $\overline{u}$ suggest a possible local correlation between $\overline{u'v'}$ and $\partial\overline{u}/\partial\phi$, especially in the vicinity of the NPJ and SPJ, consistent with a positive contribution to $C(K_E, K_Z)$ (cf Eq (10)). Figure 6 shows the point-

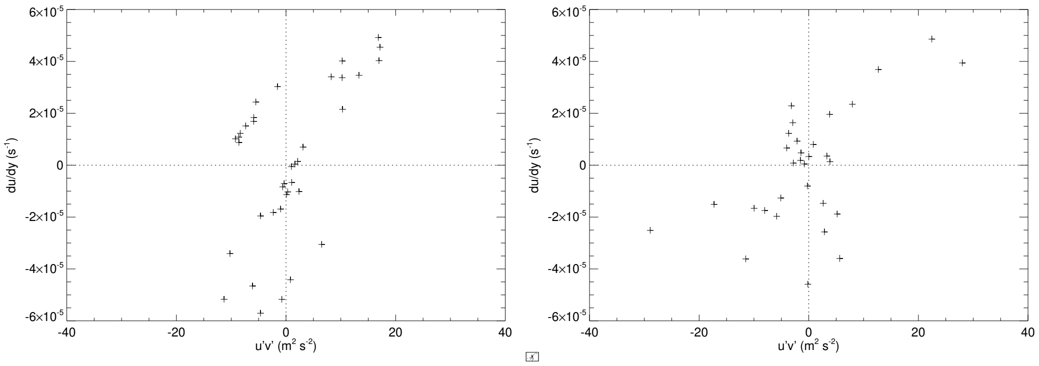

(a) Eddy momentum flux (N) u.

(b) Eddy momentum flux (S) v.

Figure 6: Pointwise scatter plots of eddy momentum flux, $\overline{u'v'}$, vs $\partial\overline{u}/\partial y$ for (a) Saturn's north polar jet region (72°-80° N and (b) the south polar jet region (66°-76° S). Both plots use a smoothing in latitude of width $\sim 1°$.

wise distribution of $\overline{u'v'}$ vs $\partial\overline{u}/\partial y = (1/a)\partial\overline{u}/\partial\phi$ for (a) the vicinity of the NPJ and (b) the SPJ ($\pm 4°$ of the jet cores). Athough there is quite a lot of scatter among the points in both jets, even by eye there is some indication of a positive correlation between $\overline{u'v'}$ and $\partial\overline{u}/\partial y$ in both frames, consistent with a positive contribution to $C(K_E, K_Z)$ in Eq (10). Calculation of the Spearman (non-parametric) rank correlation coefficient for each of the NPJ and SPJ from these data yields values of 0.36 and 0.41 respectively, indicating a rejection of the null (uncorrelated) hypothesis at the 97% and 97.5% confidence levels respectively.

Also shown in Table 1 , therefore, are the values of $C(K_E, K_Z)$ computed over latitude ranges centred respectively on the polar jets and vortices. For the polar jets, centred respectively at around 76°N and 70°S, $C(K_E, K_Z)$ is strongly positive, indicating a relatively powerful local transfer of kinetic energy from eddies into each jet at a level of at least 10^{-4} W kg^{-1}. For these features, the conversion rate into the NPJ is somewhat smaller than in the SPJ but is significantly larger in the north than the average across the rest of the north polar region. This is in contrast to the south where the conversion rate into the SPJ is similar to or slightly less than the average across the south polar region. From this calculation, however, it is not clear which scale of eddies or waves might be determining the overall rate of KE transfer into the zonal jets. In particular, the role of the north polar hexagon wave in these transfers is not clear since there are evidently waves of many differing zonal wavenumbers present across both regions.

For the polar vortices, the calculations of $C(K_E, K_Z)$ reveal major differences between the NPV and the South Polar Vortex (SPV), at least so far as their energetics are concerned. For the NPV, $C(K_E, K_Z)$ is seen in Table 1 to be significantly negative with a value around -3×10^{-5} W kg^{-1}. This would imply that eddies are gaining KE at the expense of the zonally symmetric zonal flow in the vortex, highly suggestive of a barotropic instability. Such an instability would not be unduly surprising, for example, if such polar vortices were dynamically similar in some respects to the cores of tropical cyclones on Earth, leading to the growth of elliptical or even polygonal distortions of the main vortex. For the SPV, however, $C(K_E, K_Z)$ is seen in Table 1 to be strongly positive. This would seem to suggest that the axisymmetric southern polar vortex was gaining energy from non-axisymmetric eddies, although more information, e.g. on the structure of flow, may be desirable to interpret this result.

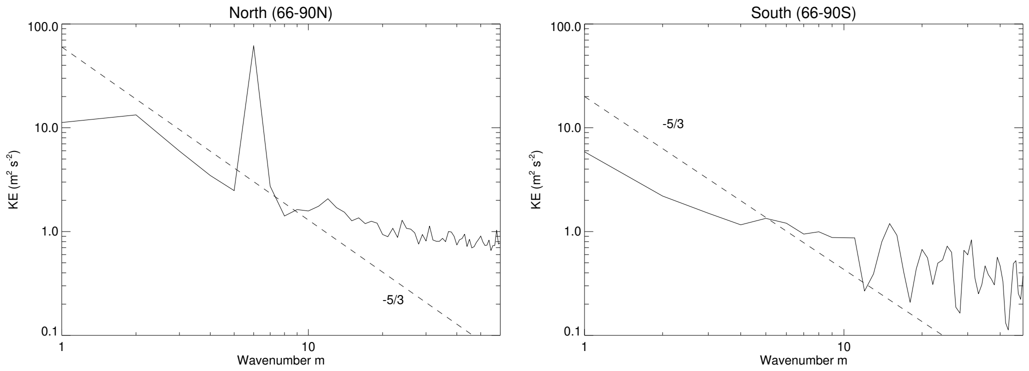

(a) EKE(m) (N). (b) EKE(m) (S)

Figure 7: Area-weighted kinetic energy spectra for (a) the northern and (b) the southern polar regions (66°–90° latitude).

4.3 Spectral decomposition

Although the simple partitioning of the flow between zonally symmetric and non-axisymmetric components allows us to determine the overall rate of KE conversion between eddies and zonal jets, this approach integrates over all eddy length scales. As a result it does not provide much insight into the roles of different zonal wavenumber components in driving or feeding barotropically off of the zonal jets. As outlined in Section 3.1 above, however, we can further decompose the flow into its zonal harmonics and thereby examine the contribution of each zonal wavenumber to the overall energy budget for the zonal jets.

Although the north polar hexagon feature is prominent in the northern polar regions, the area-averaged zonal kinetic energy spectrum (see Figure 7(a)) shows that kinetic energy is present at all zonal wavenumbers that are resolved in the observations. Thus, we see in the north a sloping continuum in the spectrum of KE with increasing m, upon which is superposed a strong peak at $m = 6$ representing the north polar hexagon. In the south, however, the spectrum appears flatter and somewhat weaker overall than in the north (see Fig. 7(b)) but still with significant EKE across all wavenumbers. The Kolmogorov -5/3 slope is indicated by dashed lines, suggesting that the northern hemisphere spectrum approaches this slope at low zonal wavenumbers but the spectrum is shallower than this at all wavenumbers in the south.

Decomposing $C(K_E, K_Z)$ into its zonal harmonics using Eq (12) we can quantify the contributions to the zonal mean KE budget due to different zonal wavenumber components. Figure 8 shows the integrand of the numerator of Eq (12),

$$C(\widetilde{K_E, K_Z})(m, \phi) = \left[\frac{\overline{u}}{a\cos^2\phi}\right]\frac{\partial}{\partial\phi}\left(\widetilde{u'v'}(m,\phi)\cos^2\phi\right), \tag{13}$$

as a function of both zonal wavenumber m and latitude ϕ for each of the north and south polar jets and polar vortices. $C(\widetilde{K_E, K_Z})(m, \phi)$ for the NPJ is clearly dominated by the contribution from the $m = 6$ hexagonal wave (Fig. 8(a)), with a strong positive contribution into the jet core and weaker negative contributions on both its northern and southern flanks. This indicates clearly that the hexagon wave itself is feeding KE into the NPJ, tending to accelerate its core and decelerating the flanks, thereby tending to sharpen the eastward jet. Contributions from other zonal harmonics are much weaker and more complicated in latitudinal structure, though a small signal at the first harmonic

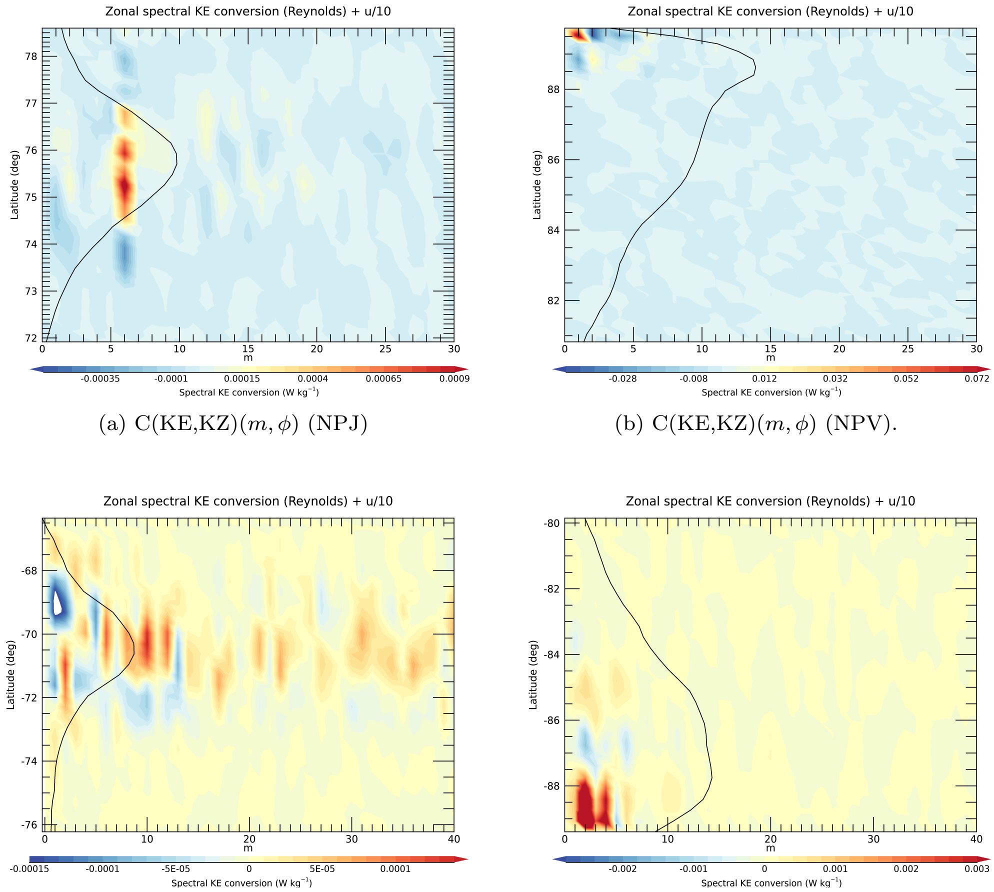

(a) C(KE,KZ)(m, ϕ) (NPJ)

(b) C(KE,KZ)(m, ϕ) (NPV).

(c) C(KE,KZ)(m, ϕ) (SPJ)

(d) C(KE,KZ)(m, ϕ) (SPV).

Figure 8: Spectrally resolved, local Eddy-zonal flow KE conversion rate, C(KE,KZ)(m, ϕ) vs zonal wavenumber m and latitude ϕ, for Saturn's north polar jet (a), north polar vortex (b), south polar jet (c) and south polar vortex (d). Note the difference in colour scales between each frame.

of the hexagon, $m = 12$, is evident among others with a weak dipolar structure in latitude.

$C(\widetilde{K_E, K_Z})(m, \phi)$ for the NPV is more complicated (see Fig. 8(b)) but is evidently dominated by contributions from low wavenumbers $m < 5$, particularly very close to the pole. The predominance of a strong contribution from $m = 1$ is somewhat surprising though images of the vortex (e.g. Antuñano et al., 2015; Sayanagi et al., 2015, and Fig. 9(a)) do appear to show some spiral cloud features and occasional secondary vortices that may break its circular symmetry. The significance of $m = 1$, however, might be indicative of a displacement of the (nearly axiymmetric) vortex away from the assumed position of the pole. Figure 9(b) shows a Cassini ISS image of the NPV with blue and green dashed circles centred on the best estimate of the position of Saturn's north pole. The red dashed circle, however, is aligned with the approximately circular cloud albedo boundary and is slightly displaced from the nearby blue latitude circle, which may indicate either a small navigation error or an actual displacement of the NPV from the north pole itself. Other significant components at $m \geq 2$ would suggest a more complex dy-

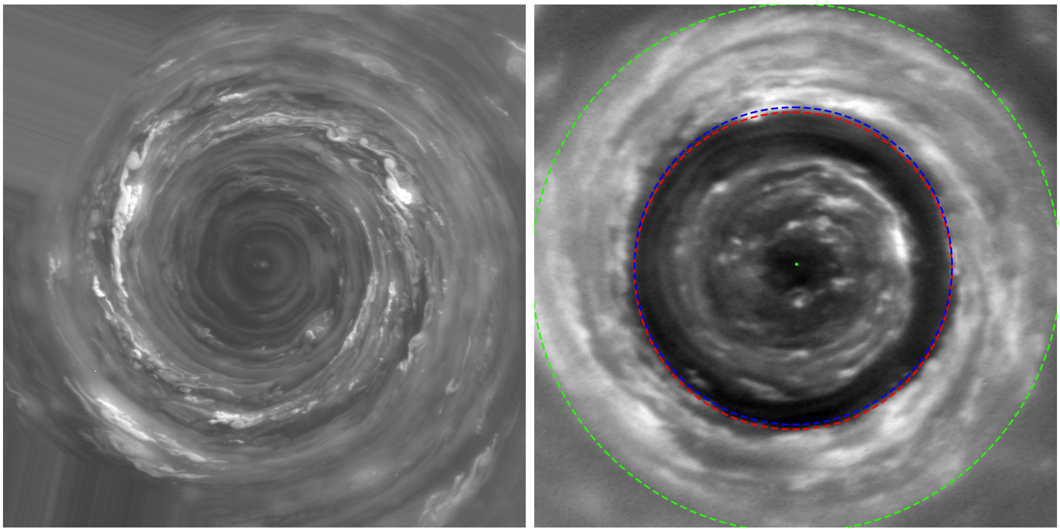

(a) (b)

Figure 9: Images of the core of Saturn's North Polar Vortex, obtained by the Cassini ISS Narrow-angle camera using the CB2 filter in (a) June 2013 and (b) April 2014. The image in (b) shows blue and green dashed circles centred on the best estimate of Saturn's north pole, while the (slightly displaced) red circle is aligned with the approximately circular cloud albedo boundary. Image scale of (a) is 5.3 km per pixel and of (b) is about 17 km per pixel. Image credits from NASA/JPL/Space Science Institute.

namical interpretation, however, possibly associated with barotropic instability of the compact vortex core.

This contrasts with the SPV, where $C(\widetilde{K_E, K_Z})(m, \phi)$ is distributed more broadly in latitude with systematic structure that is dominated by $m \geq 2$ without much of a contribution from $m = 1$ (see Fig. 8(d)). Such a predominance of $m = 2$ is consistent with the elliptical appearance of the SPV in some images (e.g. see Figure 10).

The pattern of $C(\widetilde{K_E, K_Z})(m, \phi)$ with latitude seems consistent with an acceleration of the axisymmetric vortex core within 2° of the pole from $m = 2$ and other even numbered harmonics, possibly suggestive of an acceleration of the vortex as an elliptical perturbation of the vortex decays. At lower latitudes the pattern is indicative of a tendency to flatten the outer zonal flow profile and displace a secondary peak in $\overline{u}$ at around 86°S equatorwards. Finally, $C(\widetilde{K_E, K_Z})(m, \phi)$ in the SPJ (see Fig. 8(c)) shows a systematic pattern of zonal flow acceleration from a wide range of zonal wavenumbers near the jet core, with weak deceleration on either side, mainly dominated by low wavenumbers $m \leq 10$. This pattern indicates a similar trend to the NPJ, tending to sharpen the jet and strengthen its core, but with contributions spread across a wide range of m extending almost up to the resolution limit around $m = 50$.

Integrating $C(\widetilde{K_E, K_Z})(m, \phi)$ in latitude provides a determination of the overall contribution of each zonal wavenumber component to the generation of the kinetic energy of the zonal jet flow. Figure 11 shows results obtained from area-weighted integrals of $C(\widetilde{K_E, K_Z})(m, \phi)$ over the interval in latitude within ±5° of the NPJ and SPJ respectively. This shows the clear dominance of $m = 6$ in the north in transferring kinetic energy into the NPJ (Fig. 11(a)) at a rate that is more than three times the mean conversion rate for the whole planet. $C(\widetilde{K_E, K_Z})(m)$ is also positive for many other wavenum-

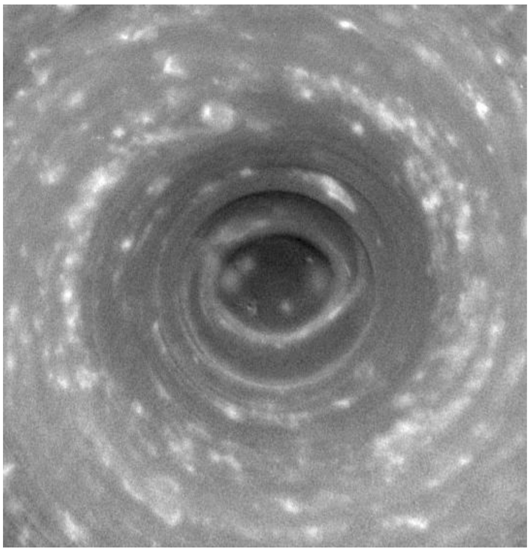

Figure 10: Image of the core of Saturn's South Polar Vortex, obtained by the Cassini ISS wide-angle camera using a spectral filter sensitive to wavelengths of infrared light centered at 752 nm on 11 October 2006. Image scale is about 17 km per pixel. Image credit from NASA/JPL/Space Science Institute, image no. PIA08332.

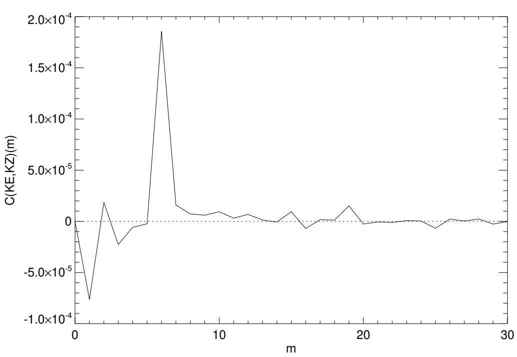

(a) C(KE,KZ)(m) (NPJ).

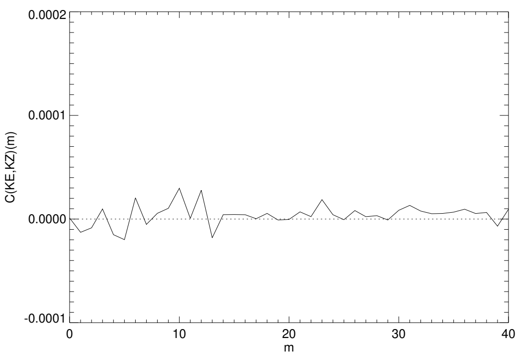

(b) C(KE,KZ)(m) (SPJ)

Figure 11: Spectrally resolved, eddy-zonal flow KE conversion rate, C(KE,KZ)(m) vs zonal wavenumber m for Saturn's north polar jet (70°–79°N) (a) and south polar jet (66°–76°S) (b).

bers, though at a much lower level. Only $m = 1, 3$ and 4 seem to show a negative conversion rate in the NPJ region, indicating that they are gaining KE at the expense of the $m = 0$ zonal jet. This focus on $m = 1$ might suggest a tendency for a slightly displaced polar vortex to move towards the planetary pole. In the SPJ, the contributions of individual wavenumber components are all relatively small in magnitude ($< 2{-}3 \times 10^{-5}$ W kg^{-1}) though predominantly positive except at $m = 1, 2, 4, 5$ and 13. However, none of these components feature particularly strongly in the zonal KE spectrum for the southern polar region (cf Fig. 7(b)).

5 Discussion

In this study we have analysed the velocity fields in Saturn's polar regions, as derived by Antuñano et al. (2015), to evaluate the interactions between nonaxiymmetric eddies, waves and zonal jet flows. The results show that, with the exception of the vortices immediately encircling the poles, the overall tendency is for eddies to transfer kinetic energy into the zonal jets via horizontal Reynolds stresses at a rate that is similar to the rest of Saturn's atmosphere at latitudes equatorwards of 60° (Del Genio et al., 2007; Del Genio & Barbara, 2012; Cabanes et al., 2020). This tendency would therefore seem to be confirmed in the atmospheres of both Saturn and Jupiter, at least at the level of the cloud tops of both planets. The earlier analysis of Antuñano et al. (2015) was unable to reach a conclusion concerning the sense of KE transfers between eddies and the zonal mean jets in the vicinity of the NPJ and SPJ because of excessive noise and scatter in plots equivalent to Fig. 6. They only considered a rather narrower latitude band than was analysed in Section 3.1 above, however, based on the raw, irregularly spaced velocity measurements. In the present analysis, some smoothing was implicit in our interpolation to a regular grid which improved the signal-to-noise ratio of the measurements, especially in the zonal mean, and the statistical analysis in Section 3.1 clearly demonstrated a statistically significant correlation consistent with a positive contribution to $C(K_E, K_Z)$.

Perhaps the most striking result of the present analysis concerns the role of the North Polar Hexagon wave in the zonal kinetic energy budget. Through our zonal spectral decomposition, it seems quite clear that the hexagon was directly transferring KE into the NPJ at a rate approaching 200 μW kg^{-1}. Unless this time period represents an unusual transient interval, therefore, when the NPH happened to be decaying and giving up its KE to the NPJ, this implies that the NPH cannot have originated as a barotropic instability of the NPJ. This would therefore rule out a whole class of explanations for the origin and maintenance of the NPH, including several recent numerical models and laboratory analogues (e.g. Aguiar et al., 2010; Morales-Juberías et al., 2011, 2015; Farrell & Ioannou, 2017). It is not clear whether this result is also inconsistent with the deep convection models of Yadav & Bloxham (2020) or Garcia et al. (2020) since they do not report on calculations of eddy-zonal flow energetics in their papers, although the zonal jets produced in such models seem strongly barotropic in character. This would certainly be of interest to calculate in further studies.

It may thus be more likely that a baroclinic instability is responsible for generating the $m = 6$ meanders in the NPJ. Several previous studies have shown that baroclinic instabilities can develop into equilibrated polygonal meanders in a vertically sheared zonal jet (e.g. Hide & Mason, 1975; Bastin & Read, 1997, 1998; Sutyrin et al., 2001; Morales-Juberías et al., 2015). In the presence of a β-effect, this can lead to kinetic energy transfers from the eddies to the zonal flow, especially if the jet width is broader than the local baroclinic Rossby radius (Held & Andrews, 1983). Conclusive confirmation of this interpretation, however, would require explicit diagnosis of the baroclinic conversion rate from potential to eddy kinetic energy, involving both the large-scale vertical velocity and temperature perturbations beneath the visible cloud tops. These are not available directly in observations, although there is some hint of a possible reversal of the northward

PV gradient with altitude close to the NPJ around the level of the cloud tops at the time of these observations in the work of Antuñano et al. (2018). One of the model simulations of Morales-Juberías et al. (2015) that reproduced a stable, hexagonal meandering jet in a shallow domain with vertical shear was also interpreted as a possible baroclinic instability, although this was not confirmed directly in other diagnostics.

The general tendency for $C(\widetilde{K_E, K_Z})(m)$ to be positive for most values of m in both the NPJ and SPJ would seem to suggest that both jets could be weakly baroclinically unstable, allowing a statistically steady trickle of KE into their parent jets via conversion from available potential energy associated with horizontal temperature gradients around and below the visible cloud tops. If this was confirmed, it would suggest an analogy between both the NPJ and SPJ and the so-called Ribbon Wave at 47° N on Saturn (e.g. Godfrey & Moore, 1986; Sayanagi et al., 2010). The reason why the NPJ develops and maintains a strong $m = 6$ wave while the SPJ does not, however, remains somewhat mysterious and may require further observations and theoretical modelling, especially perhaps with regard to the structure of the flow beneath the visible cloud tops. Such a distinction has remained elusive to most models so far, including both shallow and deep convection scenarios.

As remarked previously, the polar vortices on Saturn are distinct structures with a closed, cyclonic circulation centred quite closely on each pole (Sánchez-Lavega et al., 2006; Sayanagi et al., 2015). Images from Cassini have shown significant non-axisymmetric perturbations to both vortices in the form of waves and smaller sub-vortices (Sánchez-Lavega et al., 2006; Dyudina et al., 2008, 2009; Baines et al., 2009). The SPV in particular was seen with an elliptical ($m = 2$) distortion in the eye wall (see Fig. 10) while both the NPV and SPV exhibited spiral cloud features in their outer regions. The NPV also contained much smaller sub-mesoscale vortices embedded within the spiral cloud bands indicating some complex local instabilities. It is noteworthy that our calculations of $C(\widetilde{K_E, K_Z})(m, \phi)$ show a strong positive signal at $m = 2$ and 4 close to the south pole, consistent with the elliptical distortion of the vortex in the visible images. This would suggest that the elliptical perturbation to the vortex was actually contributing to strengthening the polar vortex itself close to its core, although further out from the core the contribution to $C(\widetilde{K_E, K_Z})(m, \phi)$ seems consistent with $m = 2$ and 4 eddies weakly forcing a secondary jet at $\sim$ 86°S northwards. In the NPV, however, $m = 2$ makes a negative contribution to $C(\widetilde{K_E, K_Z})(m, \phi)$ suggestive of its tendency to grow at the expense of the axisymmetric vortex, consistent with a barotropic shear instability, although the contribution of $m = 1$ is positive. This should perhaps be examined more closely in future work.

Similarities between both polar vortices and terrestrial tropical cyclones have been noted previously e.g. by Dyudina et al. (2009). Tropical cyclones on Earth are often observed to develop non-axisymmetric perturbations to their cores and eye walls (e.g. Schubert et al., 1999; Reasor et al., 2000; Kossin & Schubert, 2001; Kossin et al., 2002), mainly due to local transient barotropic shear instabilities, although they quickly break up and disperse on timescales of a few hours. Similar perturbations are seen in Venus's polar vortices (e.g. Limaye et al., 2009), which also show some resemblance to terrestrial tropical cyclone vortices. The perturbations to the Venus polar vortex appear also to be due to barotropic (and baroclinic?) shear instabilities (Limaye et al., 2009) which are strongly ageostrophic, much like in terrestrial cyclones where typical Rossby numbers $Ro = U/fL \sim \zeta/f$ (where ζ is the local relative vorticity) are much greater than unity. For the Saturn polar vortices, Ro is typical O(1) (Dyudina et al., 2009; Antuñano et al., 2015; Sayanagi et al., 2015), suggesting planetary rotation may be somewhat more significant for their dynamical stability. As with other atmospheric features, their origin and depth of penetration into Saturn's deep interior remain highly uncertain (cf Garcia et al., 2020). But our overall result that $C(K_E, K_Z) < 0$ for the NPV (see Table 1) is consistent with a barotropically unstable vortex at the time of the Cassini measurements. It is likely that such instabilities are, like their terrestrial counterparts, dynamically active and transient, so it would be of significant interest, to analyse cloud motions around these features at other times to obtain more statistics on the occurrence and evolution of these unstable vortices.

Acknowledgments

PLR and GC were funded by the UK Science and Technology Facilities Council (ST/N00082X/1 and ST/S000461/1). TdR and ASL were supported by the Spanish project PID2019-109467GB-I00 (MINECO/FEDER, UE) and Grupos Gobierno Vasco IT1366-19. AA was supported by a European Research Council Consolidator Grant under the European Union's Horizon 2020 research innovation programme, grant agreement number 723890, at the University of Leicester, and by the Spanish Juan de la Cierva-Incorporacion programme, grant agreement number IJC2019-040328-I/AEI/10.13039/501100011033. Gridded velocity measurements from this study will be made available via the University of Oxford Research Archive (ORA - `https://ora.ox.ac.uk/`). At the time of writing, this data has been submitted to ORA but has not yet been allocated a DOI. For review purposes, copies of the data files are included in this submission.

References

Aguiar, A. C. B., Read, P. L., Wordsworth, R. D., Salter, T., & Yamazaki, Y. H. (2010). A laboratory model of Saturn's North Polar Hexagon. *Icarus*, *206*, 755–763.

Allison, M., Godfrey, D. A., & Beebe, R. F. (1990). A wave dynamical interpretation of Saturn's polar hexagon. *Science*, *247*, 1061–1063.

Andrews, D. G., Holton, J. R., & Leovy, C. B. (1987). *Middle atmosphere dynamics.* Orlando, Fl: Academic Press.

Antuñano, A., del Río-Gaztelurrutia, T., Sánchez-Lavega, A., & Hueso, R. (2015). Dynamics of Saturn's polar regions. *J. Geophys. Res.: Planets*, *120*, 155–176. doi: 10.1002/2014JE004709

Antuñano, A., del Río-Gaztelurrutia, T., Sánchez-Lavega, A., Read, P. L., & Fletcher, L. N. (2018). Potential vorticity of Saturn's polar regions: Seasonality and instabilities. *J. Geophys. Res.: Planets*, *124*, 186–201. doi: 10.1029/2018JE005764

Archinal, B. A., & et al. (2018). Report of the IAU working group on cartographic coordinates and rotation elements: 2015. *Celest. Mech. Dyn. Astr.*, *130*, 22.

Baines, K. H., Momary, T. W., Fletcher, L. N., Showman, A. P., Roos-Serote, M., Brown, R. H., ... Nicholson, P. D. (2009). Saturn's north polar cyclone and hexagon at depth revealed by Cassini/VIMS. *Plan. Space Sci.*, *57*, 1671–1681.

Bastin, M., & Read, P. L. (1997). A laboratory study of baroclinic waves and turbulence in an internally heated rotating fluid annulus with sloping endwalls. *J. Fluid Mech.*, *339*, 173–198.

Bastin, M., & Read, P. L. (1998). Experiments on the structure of baroclinic waves and zonal jets in an internally heated rotating cylinder of fluid. *Phys. Fluids*, *10*, 374–389.

Boffetta, G., De Lillo, F., Mazzino, A., & Musacchio, S. (2011). A flux loop mechanism in two-dimensional stratified turbulence. *EPL*, *95*, 34001. doi: 10.1209/0295-5075/95/34001

Cabanes, S., Espa, S., Galperin, B., Young, R. M. B., & Read, P. L. (2020). Revealing the intensity of turbulent energy transfer in planetary atmospheres. *Geophys. Res. Lett.*, *47*, e2020GL088685. doi: 10.1029/2020GL088685

Chemke, R., & Kaspi, Y. (2015). The latitudinal dependence of atmospheric jet scales and macroturbulent energy cascades. *J. Atmos. Sci.*, *72*, 3891–3907. doi: 10

.1175/JAS-D-15-0007.1

Del Genio, A. D., & Barbara, J. M. (2012). Constraints on saturn's tropospheric general circulation Cassini ISS images. *Icarus*, *219*, 689–700.

Del Genio, A. D., Barbara, J. M., Ferrier, J., Ingersoll, A. P., West, R. A., Vasavada, A. R., ... Porco, C. C. (2007). Saturn eddy momentum fluxes and convection: First estimates from Cassini images. *Icarus*, *189*, 479–492.

Desch, M. D., & Kaiser, L. M. (1981). Voyager measurements of the rotation period of Saturn's magnetic field. *Geophys. Res. Lett.*, *8*, 253–256. doi: 10.1029/GL008i003p00253

Dyudina, U. A., Ingersoll, A., Ewald, S., Vasavada, A., West, R., Del Genio, A., ... Fletcher, L. (2008). Dynamics of saturn's south polar vortex. *Science*, *319*, 1801.

Dyudina, U. A., Ingersoll, A. P., Ewald, S. P., Vasavada, A. R., West, R. A., Baines, K. H., ... Fletcher, L. N. (2009). Saturn's south polar vortex compared to other large vortices in the solar system. *Icarus*, *202*, 240–248. doi: 10.1016/j.icarus.2009.02.014

Farrell, B. F., & Ioannou, P. J. (2017). Statistical state dynamics based theory for the formation and equilibration of Saturn's north polar jet. *Phys. Rev. Fluids*, *2*, 073801. doi: 10.1103/PhysRevFluids.2.073801

Fletcher, L. N., Orton, G. S., Sinclair, J. A., Guerlet, S., Read, P. L., Antuñano, A., ... Calcutt, S. B. (2018). A hexagon in saturn's northern stratosphere surrounding the emerging summertime polar vortex. *Nature Comms.*, *9*, 3564. doi: 10.1038/s41467-018-06017-3

Früh, W.-G., & Read, P. L. (1999). Experiments on a barotropic rotating shear layer. Part 1. instability and steady vortices. *J. Fluid Mech.*, *383*, 143–173.

Garcia, F., Chambers, F. R. N., & Watts, A. L. (2020). Deep model simulation of polar vortices in gas giant atmospheres. *Mon. Not. R. Astr. Soc.*, *499*, 4698–4715. doi: 10.1093/mnras/staa2962

Godfrey, D. A. (1988). A hexagonal feature around Saturn's north pole. *Icarus*, *76*, 335–356.

Godfrey, D. A., & Moore, V. (1986). The Saturnian Ribbon feature - a baroclinically unstable model. *Icarus*, *68*, 313–343.

Held, I. M., & Andrews, D. G. (1983). On the direction of the eddy momentum flux in baroclinic instability. *J. Atmos. Sci.*, *40*, 2220–2231.

Hide, R., & Mason, P. J. (1975). Sloping convection in a rotating fluid. *Adv. in Phys.*, *24*, 47–100.

Hueso, R., Legarreta, J., García-Melendo, E., Sánchez-Lavega, A., & Pérez-Hoyos, S. (2009). The Jovian anticyclone BA: ii. circulation and models of its interaction with the zonal jets. *Icarus*, *203*, 499–515.

Kossin, J. P., McNoldy, B. D., & Schubert, W. H. (2002). Vortical swirls in hurricane eye clouds. *Mon. Weather Rev.*, *130*, 3144–3149.

Kossin, J. P., & Schubert, W. H. (2001). Mesovortices, polygonal flow patterns, and rapid pressure falls in hurricane-like vortices. *J. Atmos. Sci.*, *58*, 2196–2209.

Limaye, S. S., Kossin, J. P., Rozoff, C., Piccioni, G., Titov, D. V., & Markiewicz, W. J. (2009). Vortex circulation on Venus: dynamical similarities with terrestrial hurricanes. *Geophys. Res. Lett.*, *36*, L04204. doi: 10.1029/2008GL036093

Montgomery, M. T., & Smith, R. K. (2017). Recent developments in the fluid dynamics of tropical cyclones. *Ann. Rev. Fluid Mech.*, *49*, 541–574. doi: 10.1146/annurev-fluid-010816-060022

Morales-Juberías, R., Sayanagi, K., Dowling, T. E., & Ingersoll, A. P. (2011). Emergence of polar-jet polygons from jet instabilities in a Saturn model. *Icarus*, *211*, 1284. doi: 10.1016/j.icarus.2010.11.006

Morales-Juberías, R., Sayanagi, K. M., Simon, A. A., Fletcher, L. N., & Cosentino, R. G. (2015). Meandering shallow atmospheric jet as a model of Saturn's north-polar hexagon. *Astrophys. J. Lett.*, *806*, L18. doi: 10.1088/2041-8205/806/1/L18

O'Neill, M. E., Emanuel, K. A., & Flierl, G. R. (2015). Polar vortex formation in giant-planet atmospheres due to moist convection. *Nature Geosci.*, *8*, 523–526. doi: 10.1038/NGEO2459

O'Neill, M. E., Emanuel, K. A., & Flierl, G. R. (2016). Weak jets and strong cyclones: Shallow-water modeling of giant planet polar caps. *J. Atmos. Sci.*, *73*, 1841–1855. doi: 10.1175/JAS-D-15-0314.1

Peixóto, J. P., & Oort, A. H. (1974). The annual distribution of atmospheric energy on a planetary scale. *J. Geophys. Res.*, *79*, 2149–2159.

Read, P. L., Conrath, B. J., Fletcher, L. N., Gierasch, P. J., Simon-Miller, A. A., & Zuchowski, L. C. (2009). Mapping potential vorticity dynamics on Saturn: zonal mean circulation from Cassini and Voyager data. *Plan. Space Sci.*, *57*, 1682–1698. doi: 10.1016/j.pss.2009.03.004

Reasor, P. D., Montgomery, M. T., Marks, F. D., & Gamache, J. F. (2000). Low-wavenumber structure and evolution of the hurricane inner core observed by airborne dual-Doppler radar. *Mon. Weather Rev.*, *128*, 1653–1680.

Sánchez-Lavega, A., del Río-Gaztelurrutia, T., Hueso, R., Pérez-Hoyos, S., García-Melendo, E., Antuñano, A., ... Wesley, A. (2014). The long-term steady motion of Saturn's hexagon and the stability of its enclosed jet stream under seasonal changes. *Geophys. Res. Lett.*, *41*, 1425–1431. doi: 10.1002/2013GL059078.

Sánchez-Lavega, A., Hueso, R., Pérez-Hoyos, S., & Rojas, J. F. (2006). A strong vortex in Saturn's south pole. *Icarus*, *184*, 524–531. doi: 10.1016/j.icarus.2006.05.020

Sánchez-Lavega, A., Pérez-Hoyos, S., Acarreta, J. R., & French, R. G. (2002). No hexagonal wave around Saturn's southern pole. *Icarus*, *160*, 216–219.

Sánchez-Lavega, A., Rojas, J. F., Acarreta, J. R., Lecacheux, J., Colas, F., & Sada, P. V. (1997). New observations and studies of Saturn's long-lived north polar spot. *Icarus*, *128*, 322–334.

Sayanagi, K. M., Baines, K. H., Dyudina, U. A., Fletcher, L. N., Sánchez-Lavega, A., & West, R. A. (2018). Saturn's polar atmosphere. In K. H. Baines, F. M. Flasar, N. Krupp, & T. E. Stallard (Eds.), *Saturn in the 21st century* (p. 337–376). Cambridge University Press. doi: 10.1017/9781316227220.012

Sayanagi, K. M., Blalock, J. J., Dyudina, U. A., Ewald, S. P., & Ingersoll, A. P. (2015). Cassini ISS observation of Saturn's north polar vortex and comparison to the south polar vortex. *Icarus*, *285*, 68–82. doi: 10.1016/j.icarus.2016.12.011

Sayanagi, K. M., Morales-Juberias, R., & Ingersoll, A. P. (2010). Saturn's Northern Hemisphere Ribbon: simulations and comparison with the meandering Gulf Stream. *J. Atmos. Sci.*, *67*, 2658–2678. doi: 10.1175/2010JAS3315.1

Schubert, W. H., Montgomery, M. T., Taft, R. K., Guinn, T. A., Fulton, S. R., Kossin, J. P., & Edwards, J. P. (1999). Polygonal eyewalls, asymmetric eye contraction, and potential vorticity mixing in hurricanes. *J. Atmos. Sci.*, *56*, 1197–1223.

Seidelmann, P. K., Archinal, B. A., A'hearn, M. F., Conrad, A., Consolmagno, G. J., Hestroffer, D., ... Williams, I. P. (2007). Report of the IAU/IAG working group on cartographic coordinates and rotational elements. *Celestial Mech. Dyn. Astron*, *98*, 155–180. doi: 10.1007/s10569-007-9072-y

Sommeria, J., Meyers, S., & Swinney, H. (1989). Laboratory model of a planetary eastward jet. *Nature*, *337*, 58–61.

Sommeria, J., Meyers, S. D., & Swinney, H. L. (1991). Experiments on vortices and Rossby waves in eastward and westward jets. In A. R. Osborne (Ed.), *Nonlinear topics in ocean physics* (pp. 227–269). Amsterdam: North Holland.

Sutyrin, G., Ginis, G. I., & Frolov, S. A. (2001). Equilibration of baroclinic meanders and deep eddies in a Gulf Stream-type jet over a sloping bottom. *J. Phys. Oceanogr.*, *31*, 2049–2065.

Sánchez-Lavega, A., Sromovsky, L. A., Showman, A. P., Del Genio, A. D., Young,

R. M. B., Hueso, R., . . . Barbara, J. M. (2019). Gas giants. In B. Galperin & P. L. Read (Eds.), *Zonal jets: Phenomenology, genesis and physics* (pp. 72–103). Cambridge, UK: Cambridge University Press.

Vallis, G. K. (2017). *Atmospheric and oceanic fluid dynamics - fundamentals and large-scale circulation (2nd edition).* Cambridge, UK: Cambridge University Press.

Vasavada, A. R., & Showman, A. P. (2005). Jovian atmospheric dynamics: an update after Galileo and Cassini. *Rep. Prog. Phys.*, *68*, 1935–1996. doi: 10.1088/0034-4885/68/8/R06

Yadav, R. K., & Bloxham, J. (2020). Deep rotating convection generates the polar hexagon on Saturn. *PNAS*, *117*, 13991–13996. doi: 10.1073/pnas.2000317117